Lamellar Diblock Copolymer Grain Boundary Morphology. 4. Tilt Boundaries

Samuel P. Gido† and Edwin L. Thomas*

Program in Polymer Science and Technology, Department of Materials Science and Engineering, Massachusetts Institute of Technology, Cambridge, Massachusetts 02139

Received February 15, 1994; Revised Manuscript Received July 9, 1994®

ABSTRACT: Tilt grain boundaries in poly(styrene-*b*-butadiene) lamellar diblock copolymers were characterized using transmission electron microscopy (TEM). Three distinct tilt grain boundary morphologies were observed: the chevron, the omega boundary, and the T-junction. All three boundary types are found to have intermaterial dividing surfaces, separating the polystyrene and polybutadiene microphases, that approximate surfaces of constant mean curvature. The chevron and omega morphologies are observed for symmetric tilt boundaries, and a transition occurs from the chevron to the omega as tilt is increased at constant boundary width. A transition from either the chevron or the omega boundary to the T-junction occurs as the boundary becomes more asymmetric. Analyses of both of these transitions using geometrical arguments are in agreement with experimental observations.

Introduction

Diblock copolymer materials that form microphase-separated morphologies such as spheres, cylinders, the ordered bicontinuous double diamond (OBDD), and lamellae also form larger scale grain structures.[1,2] Block copolymer grain structure and grain boundary morphology have been found to have important effects on the mechanical and transport properties of these materials.[3,4] This is the final paper in a four-part series that focuses on grain boundary structures in poly(styrene-*b*-butadiene) diblock copolymers (SB).

In the first paper,[1] which we will refer to as GB-I (grain boundary I), the twist and tilt degrees of freedom for grain boundaries were defined and twist boundary morphology was characterized by transmission electron microscopy (TEM). Two twist boundary morphologies were observed: the Scherk surface twist boundary and the helicoid section boundary. In the second[2] and third[5] papers of this series, which we will refer to as GB-II and GB-III, two different methods for calculating twist grain boundary energies for the Scherk (GB-II) and helicoid section (GB-III) boundaries were used: (1) a self-consistent field approach and (2) integrating a continuum elasticity expression for the free energy density as a function of interfacial curvature over the complicated interfacial geometry. This fourth paper will concentrate on both the characterization and modeling of *tilt* grain boundaries.

The experimental details of sample preparation and characterization by transmission electron microscopy (TEM) for this tilt boundary study are the same as those described in GB-I for the twist boundary study. The block copolymers used are again the symmetric poly(styrene-*b*-butadiene) (SB) diblock copolymers with polystyrene/polybutadiene compositions of 20500/20500, 42300/45400, and 81000/74700 g/mol (designated SB 20/20, 40/40, and 80/80). In TEM micrographs the PB domains appear dark due to staining with OsO_4, while the PS domains appear light.

Figure 1 illustrates the degrees of freedom necessary to characterize pure tilt grain boundaries. The tilt of the boundary is quantified by the angle θ, measured between the normals to the two sets of lamellae on either side of the boundary. The PB and PS domains are separated by an intermaterial dividing surface (IMDS). As in GB-I, the intermaterial dividing surfaces in the grain boundary regions and in other defect structures will be designated IMDS† to distinguish them from the interfacial surfaces in equilibrium microdomain morphologies, which are designated IMDS. Figure 1a shows the geometry of a symmetric tilt boundary. The boundary plane, shown as a bold line, is symmetrically located, bisecting the angle θ. In Figure 1b the placement of the boundary plane is no longer symmetrical; the deviation from symmetry is

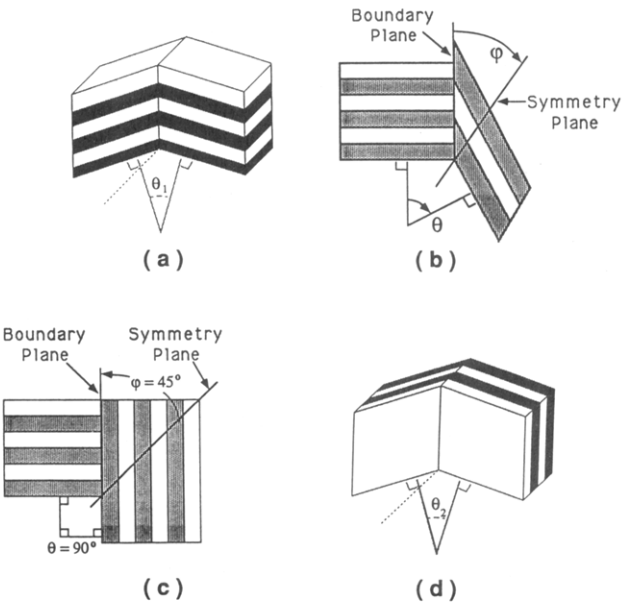

Figure 1. Tilt grain boundary geometry. (a) Symmetric tilt boundary. The tilt angle θ is measured between the perpendiculars to the two sets of lamellar planes. (b) When the placement of the boundary plane is no longer symmetrical, the deviation from symmetry is quantified by the angle, φ, between the boundary plane and the plane of symmetry which bisects θ. (c) The pure T-geometry occurs when $\theta = 90°$ and $\varphi = 45°$. (d) By comparison to part a, it can be seen that only the component of tilt measured in the plane that is simultaneously perpendicular to both sets of lamellar planes on both sides of the boundary is observable. The tilt misorientation shown does not produce a grain boundary.

*To whom correspondence should be addressed.
† Present address: Department of Polymer Science and Engineering, University of Massachusetts, Amherst, MA 01003.
® Abstract published in *Advance ACS Abstracts,* September 1, 1994.

0024-9297/94/2227-6137$04.50/0

quantified by the angle φ. When $\theta = 90°$ and $\varphi = 45°$, the special case illustrated in Figure 1c occurs, which we will call a pure T-geometry. Here the two sets of lamellae are perpendicular at the grain boundary plane. In general, the degrees of tilt freedom, θ and φ, each occur in two orthogonal planes, yielding a total of four degrees of geometrical freedom. (An additional degree of freedom we do not consider is relative translation of lamellae parallel to the boundary.) However, Figure 1d indicates that only the components of tilt and asymmetry measured in the plane that is simultaneously perpendicular to both sets of lamellar planes on both sides of the boundary are observable in lamellar tilt boundaries due to the two-dimensional nature of the domains.

As with twist grain boundaries, it will be shown that in the case of the pure tilt boundary there are competing morphologies: the chevron, the omega, and the T-junction. A transition from the chevron morphology to the omega morphology is observed as the tilt angle, θ, increases at constant boundary width or alternatively as boundary width is decreased at constant tilt. This transition occurs through boundaries which have intermediate character between the chevron and omega. Both the chevron and the omega boundaries, which are symmetric ($\varphi \approx 0°$), undergo a transition to the T-junction when the boundaries become highly asymmetric (φ increases). It will be shown experimentally and through geometrical calculations that in tilt boundaries these different morphologies and the transitions between them result from the need to satisfy geometrical constraints to which the boundaries must conform.

GB-II contains a discussion of possible mechanisms of grain boundary formation in lamellar diblock copolymers. These include impingement of growing grains during a first-order phase transition, the distortions of the lamellar phase by disclination line defects (i.e., focal conic textures), and the formation of kink bands due to compressive stresses that may be generated as the solvent is removed during the sample casting process. Kink bands are of special interest here because they generate only pure tilt boundaries (no twist component). Pairs of tilt boundaries of approximately equal but opposite tilt are formed in long parallel kink bands. This type of structure is evident in an upcoming figure (Figure 6) and in the boxed region of GB-II Figure 2.

Tilt Boundary Morphologies: Chevron, Omega, and T-Junction

Figure 2 shows TEM micrographs of the three general types of tilt boundaries observed in lamellar diblock copolymers. A *chevron* tilt boundary where the lamellae bend continuously across the grain boundary is shown in Figure 2a. A second type of continuous tilt boundary, shown in Figure 2b, is a variant of the chevron in which the lamellae in the grain boundary region go through a bend which approximates the shape of the capital Greek letter Ω. This *omega* type tilt boundary is observed at higher tilt angles. Finally, Figure 2c shows a discontinuous tilt boundary called the *T-junctions*, where the lamellar planes on one side of the boundary terminate. In this type of boundary the continuity of the lamellar planes across the grain boundary is disrupted. T-junction boundaries are only rarely observed. In the language of smectic liquid crystals the chevron and omega boundaries are tilt walls while the T-junction might be described as a dissociated tilt wall.[6,7]

TEM images of tilt boundaries were observed to compile statistics on boundary geometries for the three different

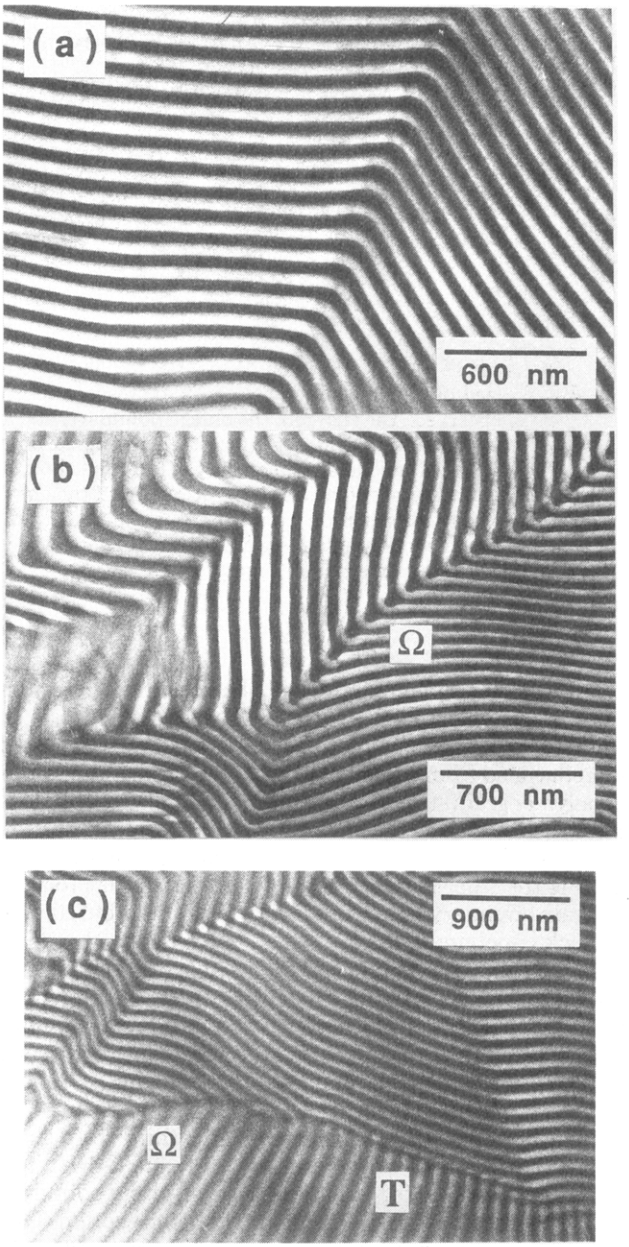

Figure 2. Tilt boundary morphologies in SB 80/80. (a) Chevron tilt boundary: The lamellae bend continuously across the grain boundary. (b) Omega tilt boundary, labeled Ω in the figure. (c) T-Junction tilt boundary: On the right-hand side, labeled T, the boundary has a pure T-geometry, and there is a break in lamellar continuity at the boundary. On the left-hand side, labeled Ω, the boundary has the same tilt angle of approximately 90°, but it becomes symmetric and displays the omega morphology.

molecular weights. The tilt angle and boundary width, W, were measured from TEM negatives and the morphology type was noted. Of 160 boundaries characterized in SB 20/20, 40/40, and 80/80, only 6 were T-junctions. Figure 3 shows schematic diagrams of the chevron, omega, and T-junction tilt boundary geometries. All three types of boundaries represent a local disturbance of the lamellar order which is concentrated into a region of width W. Figure 3a is a schematic diagram of a chevron tilt boundary. Based upon images such as Figure 2a, it is reasonable to model these boundaries using constant mean curvature semicylinders, which are shown in cross section in the figure as semicircular arcs. The angle of such an arc (measured between the normals to the two sets of lamellae), θ, is given by the required boundary geometry, while the radius, R, is related to the observed boundary width by the

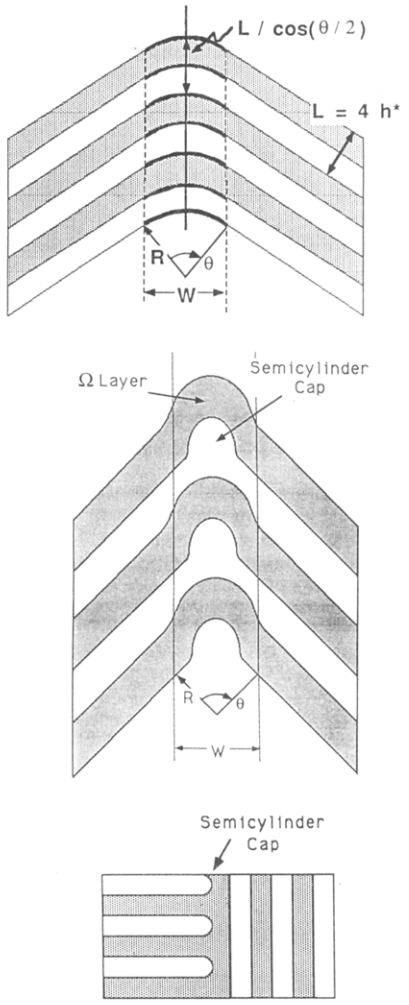

Figure 3. Schematic diagrams of tilt boundary morphologies. (a) Chevron tilt boundary. The tilt angle, θ, the radius of curvature, R, and the boundary width, W, are indicated. The lamellar long period L increases to $L/\cos(\theta/2)$ at the center of the boundary region. The equilibrium flat layer thickness, h^*, is one-quarter of the long period. The layer thickness increases from its equilibrium value in the boundary region. (b) Omega tilt boundary. One lamellar layer forms a semicylindrical cap at the center of the boundary while the other layer covers this protrusion in an Ω-shaped layer. (c) T-Junction tilt boundary. There is a lack of lamellar continuity across this boundary type. The PS lamellae on the left-hand side of the boundary end in semicylindrical caps.

geometrical formula

$$R = W/2 \sin(\theta/2) \quad (1)$$

The structure of the omega boundary, shown in Figure 3b, is more complex. There is a protruding bump of one of the two lamellar phases at the center of the chevron-like bend. The IMDS† that separates this protrusion from the next lamellar layer is approximately half of a cylinder. This inner protrusion is then covered by the next lamellar layer. This covering layer is distorted from the chevron type geometry into an Ω shape by the presence of the inner protrusion. It does not seem to matter which microdomain, PS or PB, forms the inner protrusion and which forms the covering layer. Figure 4 shows an omega boundary in which the roles of the two microdomains switch along the boundary. On the left-hand side of the boundary, PS forms the inner protrusion and PB the outer covering layer, but these roles are reversed on the right-hand side of the same boundary. It is evident in the TEM micrographs and in the schematic illustration, Figure 3b, that the omega

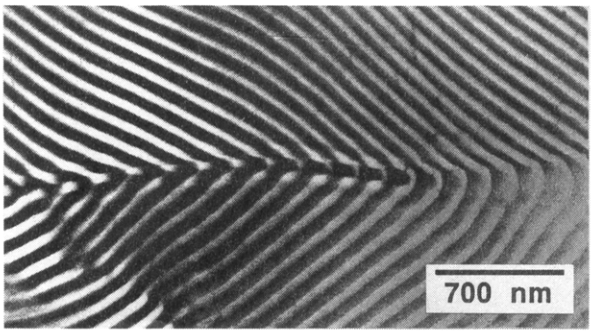

Figure 4. Omega tilt boundary in SB 80/80 in which the PS and PB domains switch roles of protrusion and omega layer. On the left-hand side of the boundary, PS forms the inner protrusion and PB the outer Ω layer. These roles are reversed on the right-hand side of the boundary.

morphology leads to both sharp interfacial curvatures and distortions of the lamellar layers from their equilibrium thickness. No doubt there are energetic penalties for these distortions. However, it will be shown in the next section that geometric constraints imposed on the boundary by the tilt misorientation necessitate the formation of the omega morphology despite the fact that its energy is obviously higher than the energy of the chevron morphology.

In Figure 5 the ratio of the experimentally observed boundary width to the lamellar long period, W/L, is plotted vs tilt angle for the two types of continuous tilt boundaries: chevron and omega. Parts a–c of Figure 5 show plots for SB 20/20, 40/40, and 80/80, respectively. In each graph the squares represent chevron boundaries, the circles represent omega boundaries, and the triangles represent boundaries that appear to be intermediate between the chevron and omega morphologies. Figure 6 shows such an intermediate boundary with a partially formed protrusion. There are actually three parallel tilt boundaries in this micrograph which were probably formed by a mechanical buckling process. The upper one of these three boundaries shows the strongest intermediate character.

For all three molecular weights only chevrons are observed at lower tilt angles. At higher tilts, a transition is observed passing through the intermediate boundaries until omegas predominate at the highest tilt angles observed. The transition from chevrons to omegas for each molecular weight occurs over a range of tilt angles in which both morphologies are observed as well as boundaries of intermediate character. For SB 20/20, the transition range is 80–105°; for 40/40, the transition range is 70–85°; and for 80/80, the transition range is 65–80°. The curve which, on all three plots, passes approximately through the transition region is a theoretical prediction of the transition from the chevron to the omega morphology which will be explained in the next section.

For all three molecular weights, the W/L data are scattered over a range of about 1 long period. Thus, boundary widths appear to be approximately independent of tilt angle. Due to the relationship between R and W given by eq 1, a constant W/L implies an increasing R with decreasing tilt angle. The mean curvature of the chevron IMDS† ($H = 1/(2R)$) thus decreases with decreasing tilt, approaching zero as tilt approaches zero. The average boundary widths for the three different molecular weights, taken over all the boundary types, are $W/L = 1.41$, 0.84, and 0.91 for SB 20/20, 40/40, and 80/80, respectively. Given the scatter of the data, the difference between the SB 40/40 and 80/80 average W/L values is not considered significant. However, the SB 20/20 W/L average value is clearly higher than the other two. We currently have no

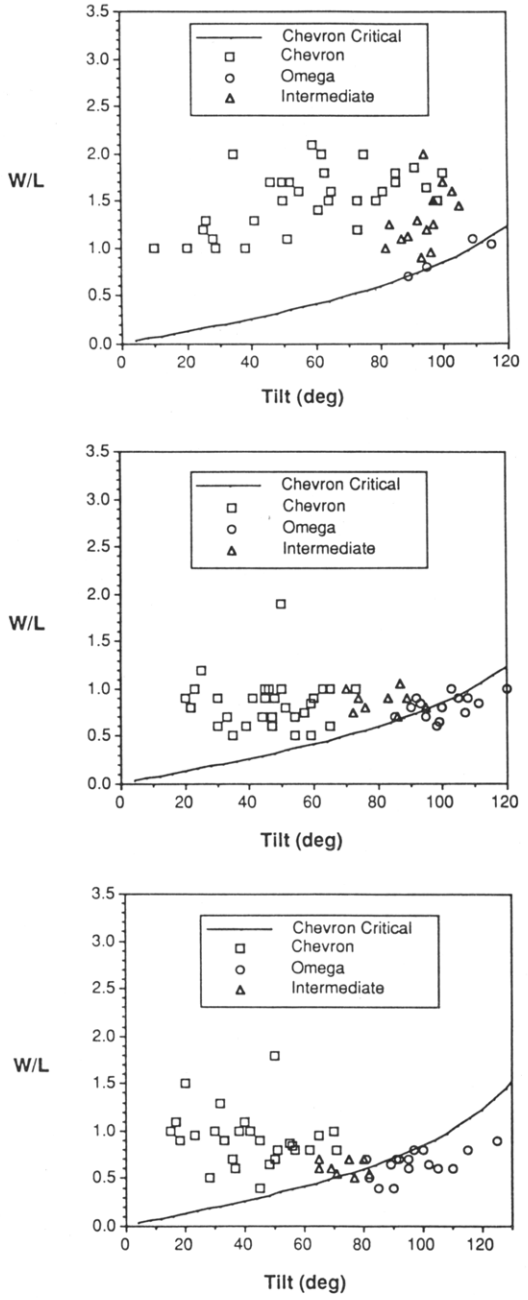

Figure 5. Symmetric tilt boundary width, W/L, vs tilt angle. The squares represent chevron boundaries, the circles represent omega boundaries, and the triangles represent boundaries of intermediate chevron/omega character. (a) SB 20/20; (b) SB 40/40; (c) SB 80/80. In all three graphs the line curve represents the critical condition for chevron stability.

explanation for these trends in average W/L for the different molecular weights. However, the greater W/L values in SB 20/20, regardless of how they come about, are responsible for pushing the transition from the chevron to the omega morphology to higher tilt angles, as will be explained in the next section.

Chevron and Ω Tilt Boundary Geometry and Energy Considerations

As discussed in GB-II a continuum elastic interface model leads to the following form of the free energy per unit area, f, of a diblock copolymer interface:

$$f = f_0 + kH^2 + \bar{k}K \qquad (2)$$

This expression is for the particular case, relevant to our diblock copolymer lamellar systems, in which the natural or preferred curvature of the layers is zero (flat planes). Here, f_0 is the free energy per unit area of the minimum energy flat diblock interface, while H and K are mean and Gaussian curvatures which characterize the deviation from the flat case. k is the splay modulus and $\bar{k}$ is the saddle-splay modulus. The determination of these two moduli by Wang and Safran[8,9] is discussed in GB-II, where values are given for SB 20/20, 40/40, and 80/80. For the semicylindrical IMDS†'s observed in the chevron tilt boundaries, K is equal to zero and H is a constant equal to $1/(2R)$.

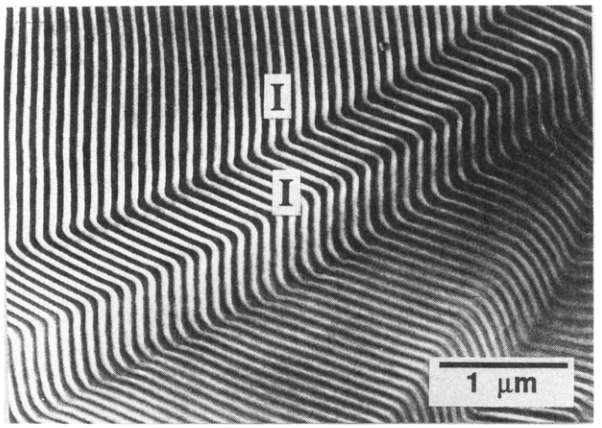

Figure 6. Boundaries in SB 80/80 of intermediate character between the chevron and omega morphologies, labeled I. The three parallel tilt boundaries in this figure were probably formed by a mechanical kinking process. The upper of the three boundaries shows the strongest intermediate character, although the middle boundary is also clearly intermediate.

As discussed in GB-II, Wang and Safran's implementation of the type of energy relationship shown in eq 2 is strictly applicable only to an isolated diblock layer. It assumes that the only important energy contributions are interfacial and chain stretching energies and that the single diblock layer is subject to no external constraints other than the curvature that the layer is assumed to possess. The twist boundary morphologies discussed in GB-II and GB-III impose additional geometric constraints that alter the curvature-induced energies from those predicted by Wang and Safran. In these cases it was necessary to solve a more involved self-consistent field (SCF) problem to take these additional constraints into account. In the chevron tilt boundary morphology there is also an additional constraint due to the grain boundary geometry, which will be shown to have an impact on IMDS† curvature.

Through conservation of volume the interfacial area per chain, Σ, is directly linked to the height, h, of the grafted layer. Parts a–c of Figure 7 show a piece of diblock interface as tilt increases and the morphology changes from a flat interface to a chevron boundary, to an intermediate boundary, and eventually to an omega boundary. The diblock chains tethered to this curved IMDS† can be assigned imaginary volume elements as shown in Figure 7. A polymer chain is drawn in the central element to illustrate this. The sides of these volume elements are all normal to the IMDS† at their points of contact, and the total volume of each element is equal to the volume of a chain. A volume element has area Σ at the interface. The area of a two-dimensional slice through a volume element parallel to the surface at a height z above the surface is $\Sigma(z) = (1 + zc_1)(1 + zc_2)\Sigma = (1 + 2Hz + Kz^2)\Sigma$. The conservation of volume constraint for a single chain is[10]

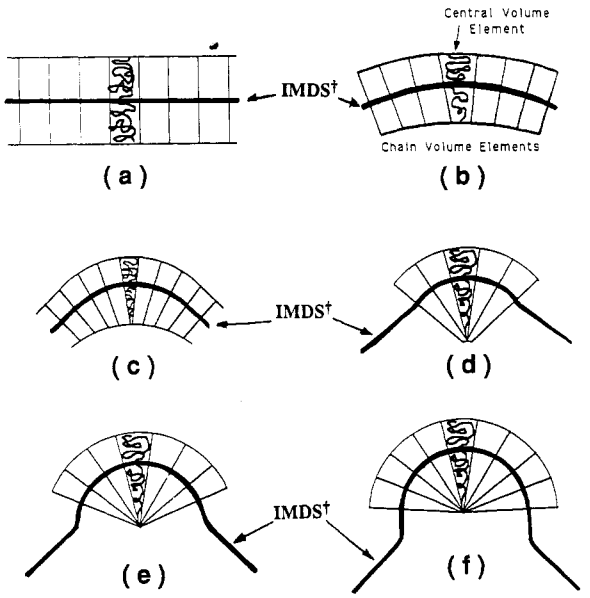

Figure 7. Chain volume element geometry as a function of tilt angle. In all parts of this figure the central volume element has a polymer chain drawn in it. (a) When the IMDS† is flat, the volume elements are rectangular parallelpipeds. (b) For low to moderate curvature, the central volume element becomes a section of an annulus. The adjoining elements are similarly deformed. (c) At some critical combination of W and tilt angle, the central volume element is the first element to reach a wedge-shaped geometry. This is the upper tilt angle limit of the chevron morphology for a given W. (d) On further increasing the tilt angle, above the chevron critical condition, volume elements adjacent to the central element also become wedge shaped, leading to the start of a protrusion. Such boundaries are termed of intermediate character. (e) At still higher tilt, enough volume elements are wedge shaped to complete a full semicylindrical protrusion. (f) For even higher tilt angles, above about 110°, the protrusion must elongate into an extra lamellar half-plane to fulfill the required lamellar spacing at the center to the tilt boundary.

$$\int_0^h \Sigma(z)\,dz = N_A\nu \tag{3}$$

where N_A is the degree of polymerization of the block on the side of the interface under consideration and ν is the volume per monomer. Thus the product $N_A\nu$ is the volume of the A block. This integral may be evaluated to yield a cubic equation relating h and Σ:

$$\frac{1}{3}Kh^3 + Hh^2 + h - \frac{N_A\nu}{\Sigma} = 0 \tag{4}$$

For the cylindrically based chevron model $K = 0$, so the first term in eq 4 becomes zero. The minimal surface IMDS†'s previously encountered with the twist boundary modeling in GB-II and GB-III had the property that the curvature environments on both sides of the IMDS† were equivalent. However, in the present case, the cylindrically shaped IMDS† creates different curvature environments experienced by chains on the concave and convex sides of the interface. Equation 4 must be solved separately for the concave side of the IMDS† to yield the brush height on this side, h_{cc}, and for the convex side to yield h_{cv}. The mean curvature, H, is assigned a positive value when viewed from the convex side of the interface and a negative value when viewed from the concave side. The coordinate z in eq 3, however, is always taken as a positive value of the distance from the IMDS† whether on the concave or convex side. In a diblock copolymer the two blocks, one on the concave side and one on the convex side, must share a common Σ.

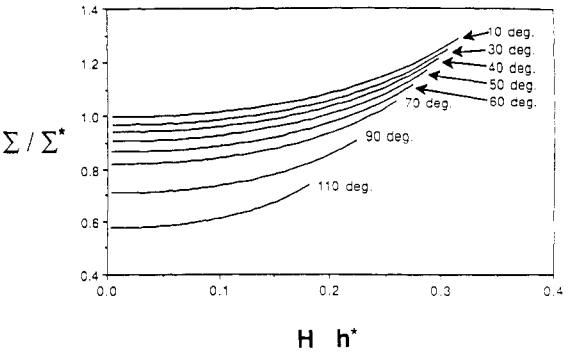

Figure 8. Plots of Σ/Σ^* (the ratio of the interfacial area per chain in the central element of the chevron morphology to the flat interface area per chain) vs the dimensionless product of the mean curvature and brush height, Hh^*. Curves are shown for tilt angles ranging from 10 to 110°.

Reexamining the chevron boundary geometry (recall Figures 2a and 3a), notice that the lamellar spacing becomes larger in the curved region than in the adjoining flat lamellae. This is the result of the necessity of completely filling space under the geometric constraints imposed by the grain boundary. If we assume a symmetric diblock copolymer so that in the flat lamellar case both blocks exhibit the same equilibrium brush height, h^*, then in the chevron boundary the lamellar spacing at the center of the bend becomes $2h^*/\cos(\theta/2)$. At the center of the bend, the sum of the convex and concave brush heights must equal this spacing. Thus the grain boundary geometry imposes the following additional constraint:

$$h_{cc} + h_{cv} = 2h^*/\cos(\theta/2) \tag{5}$$

For a given tilt angle eqs 4 and 5 are solved simultaneously to yield a relationship linking possible combinations of H and Σ which satisfy the geometric constraints for a given tilt angle, θ:

$$\frac{4Hh^*}{\cos(\theta/2)} = \left(1 + \frac{4HNa^3}{\Sigma}\right)^{1/2} - \left(1 - \frac{4HNa^3}{\Sigma}\right)^{1/2} \tag{6}$$

Figure 8 shows dimensionless plots of Σ/Σ^*, where Σ^* is the flat interface area per junction, vs Hh^* for tilts ranging from 10 to 110°, obtained by solution of eq 6. The important feature is that the area per junction on the interface in the chevron boundary decreases with increasing tilt. This is because, through eq 5, it is apparent that increasing tilt requires an increase in the lamellar spacing in the grain boundary region. The central volume element in Figure 7 must therefore increase in height. Because volume is conserved, an increase in volume element height must lead to a decrease in Σ. At a given tilt angle, Figure 8 also shows that Σ/Σ^* increases with increasing Hh^*. This trend is due to the shape change in the volume element per chain illustrated in Figure 7. Equations 5 and 6 apply specifically to a volume element situated at the center of the chevron bend. In all parts of Figure 7, this central volume element contains a sketch of a polymer chain; neighboring elements are also shown but without chains. For the flat interface all the chain volume elements are rectangular boxes, as shown in Figure 7a. When the interface is curved into a cylindrical geometry, the shape of the volume element initially changes into a section of an annulus at small to moderate curvatures, as shown in Figure 7b. Finally, as curvature continues to increase, the central element is the first to reach a wedge-shaped geometry (Figure 7c). Because segmental density remains constant, the volume of the element must remain the same

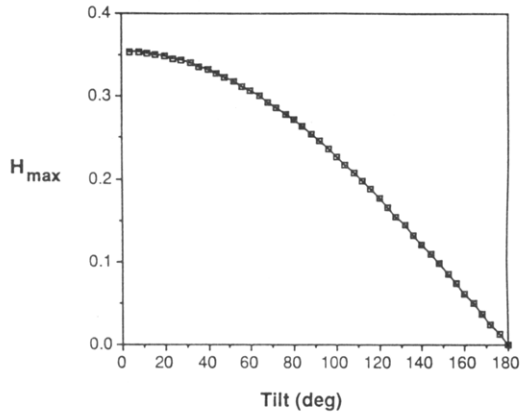

Figure 9. Plots of H_{max}, the maximum mean curvature for which the chevron morphology can occur, vs tilt angle. For higher curvatures the boundaries undergo the transition to the omega morphology.

during this transformation. This necessitates an increase in the surface area with which the element contacts the interface.

Notice in Figure 8 that the Σ/Σ^* vs Hh^* curves end at lower Hh^* values as the tilt angle increases. The points at which these curves end represent the situation shown in Figure 7c, where the central volume element becomes a wedge shape. It is not possible to increase the interfacial curvature any farther than this while still maintaining the chevron geometry. The value of H for which this situation is reached decreases with increasing tilt and can be found from the limit of applicability of eq 6. The limit of physical applicability of eq 6 is reached when $1 = 4HNa^3/\Sigma$. Thus the equation that yields the end points for the curves in Figure 8 is

$$4Hh^*/\cos(\theta/2) = \sqrt{2} \tag{7}$$

The limit of applicability of eq 6, given by eq 7, represents a point at which the chevron model breaks down. Figure 9 plots the highest curvature attainable in the chevron geometry, H_{max}, vs tilt angle. The smallest attainable radius of curvature for a given tilt angle is then given by $R_{min} = 1/(2H_{max})$. Through eq 1, R_{min} is related to the minimum grain boundary width for which the chevron boundary can occur at a given tilt angle, W_{min}. The previously mentioned curves in Figure 5a–c are plots of W_{min}/L vs tilt angle. As the experimental data approach and then cross these curves, the nature of the observed tilt boundaries changes from chevron to intermediate and finally to omega. The reason for this is illustrated in Figure 7c–e. As previously stated, Figure 7c represents the limit of applicability of the chevron model. For a smaller W at the same tilt or for a larger tilt angle at the same W, the situation illustrated in Figure 7d must develop in order to continue to achieve the required $2h^*/\cos(\theta/2)$ lamellar spacing at the center of the bend. Here some of the chain volume elements adjacent to the central element also become completely wedge shaped. This leads to a slight protrusion in the center of the chevron bend, thus giving a boundary of intermediate chevron/omega character. If W is decreased further or tilt is increased further, then as shown in Figure 7e a sufficient number of the chain volume elements in the center of the boundary become wedge shaped to form a full semicylindrical protrusion. Parts a and b of Figure 10 show two tilt boundaries, one in SB 20/20 (Figure 10a) and one in SB 80/80 (Figure 10b), where W changes along the boundary. In both boundaries, W increases and a transition is observed from an omega to intermediate to chevron morphology. Also notice that

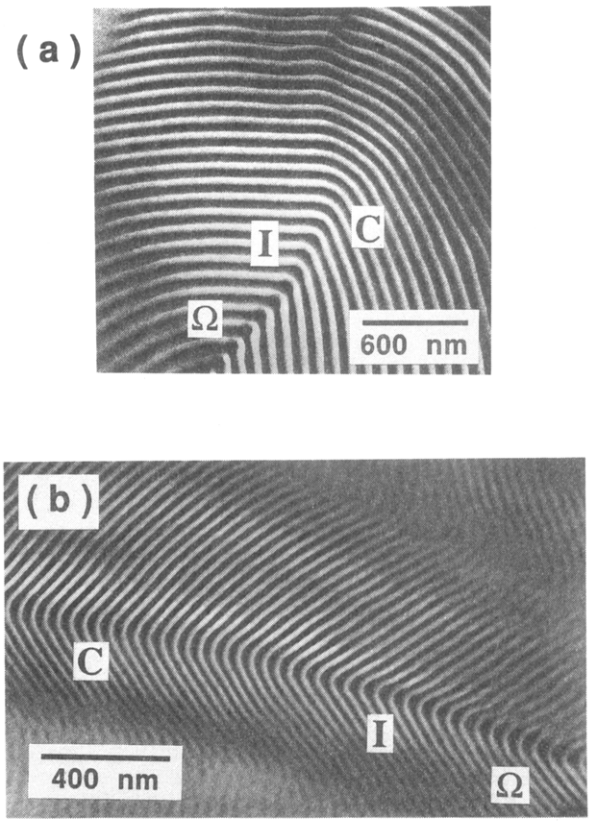

Figure 10. Symmetric tilt boundaries that undergo a continuous transition from the chevron (labeled C), through an intermediate (labeled I), to the omega morphology (labeled Ω) due to a change in boundary width, W. (a) SB 20/20; (b) SB 80/80.

the boundary width W/L, measured in the long period of the appropriate diblock, is significant larger in the SB 20/20 sample.

As tilt angle continues to increase above the point where the semicylindrical protrusion of the omega boundary is fully formed, the protrusion is no longer sufficient to fill the required spacing distance at the center of the boundary. In this case, shown in Figure 7f, the protrusion can continue to grow by developing into a short lamellar section with a semicylindrical cap. The simple semicylindrical protrusion of Figure 7e is sufficient to achieve the required lamellar spacing in the grain boundary region up to tilt angles of about 110°. Boundaries with higher tilt angles than this are only rarely observed. Figure 11 shows a TEM micrograph of one of these rare very high angle omega tilt boundaries in SB 80/80. In the lower portion of the boundary the tilt angle is 125°, and the elongated protrusions as in Figure 7f are clearly visible. Notice that within this high-tilt region that the material which forms the protrusion changes from PS in the lower part to PB in the upper part. Higher up still, the tilt boundary divides into two lower angle tilt boundaries, 89 and 28°, labeled Ω and C1, respectively. The combination of these two lower angle boundaries achieves approximately the same tilt reorientation as the higher angle boundary below. High-angle tilt boundaries are commonly observed splitting into two lower angle boundaries like this (such a split is also seen in Figure 2b). The 89° tilt boundary has an omega morphology with a semicylindrical cap as in Figure 7e, while the 28° boundary is a chevron.

The experimental data in Figure 5 show the transition from chevron to intermediate to omega tilt boundary types to be in very good agreement with the position of the W_{min}/L curve, especially considering that the assumption of equal domain thicknesses and chain volumes used in

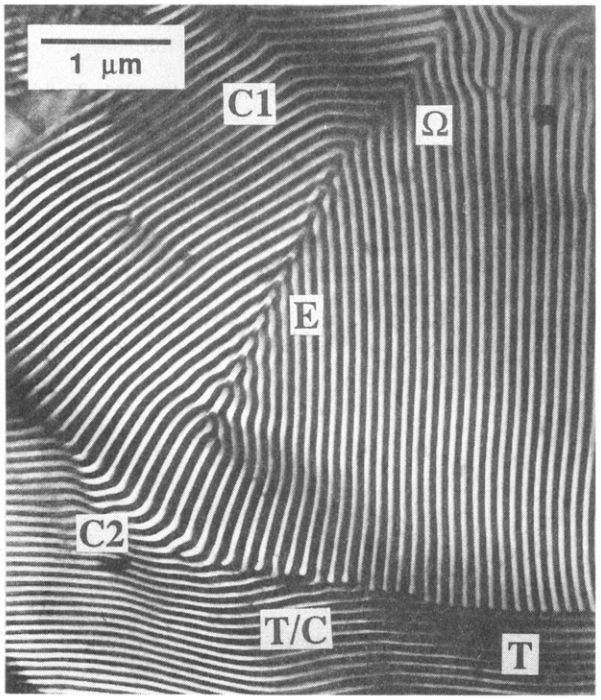

Figure 11. TEM micrograph of SB 80/80 displaying a number of tilt boundaries of various morphology. In the center of the micrograph, labeled E, is a 125° angle symmetric tilt boundary. At this very high tilt angle, the protrusion of the omega boundary becomes elongated into an extra lamellar half-plane. Toward the top of the micrograph, this omega boundary splits into two lower angle boundaries: an 89° omega boundary, labeled Ω, and a 28° chevron boundary, labeled C1. Together these two lower angle boundaries achieve approximately the same tilt reorientation as the higher angle tilt boundary below. In the lower right-hand corner of the micrograph is a T-junction boundary, labeled T, that displays the pure T geometry. Proceeding to the left along this boundary, the boundary becomes more symmetric and a transition occurs to the chevron morphology, labeled C2. In the region of the gradual transition between the T-junction and the chevron, labeled T/C, some lamellar planes terminate in T-junction fashion while others make the bend across the boundary like a chevron.

this calculation are only approximations. We do not know why the SB 20/20 tilt boundaries had, on average, larger W/L values. However, this causes the SB 20/20 data to cross the W_{min}/L curve at a higher tilt angle. We believe that is responsible for SB 20/20 displaying a significantly higher experimentally observed tilt angle range for the chevron to omega transition than either SB 40/40 or 80/80.

T-Junction Boundaries

The lower right-hand portion of the micrograph in Figure 11 contains another tilt boundary, a T-junction. A schematic illustration of the T-junction morphology is shown in Figure 3c. These boundaries are only very rarely observed and tend to occur when there is a combination of a high tilt angle, θ, and a high asymmetry angle, φ. In this micrograph $\theta \approx 90°$ and $\varphi \approx \theta/2 \approx 45°$, which is the condition for a pure T-geometry.

Arguing in terms of a free energy relationship such as that given by eq 2, it is clear that the energy per chain in the T-junction morphology must be higher than in the symmetric chevron boundaries ($\varphi = 0$) discussed in the previous section. The interfacial curvature in the chevron boundaries is always much less than that in the cylindrical caps that terminate the PS lamellae in the T-junction in Figures 2c, 3c, and 11. The energy penalty for the increasing mean curvature of the IMDS†, as modeled by Wang and Safran, includes both an increase in chain conformational energy and an increase in interfacial area per chain. Notice in Figures 2c and 11 that the cylindrically capped ends of the PS lamellae are slightly enlarged. This enlargement is likely due to an energetic drive to reduce the unfavorable interfacial curvature by enlarging the radius of the semicylindrical cap.

When the asymmetry angle, φ, becomes large, as shown in Figure 1b, the chevron morphology experiences a geometrical difficulty; the lamellae cannot match up across the boundary. In the case illustrated in the figure, the left-hand set of lamellae approach the central plane of the boundary with a repeat distance of L, the true long period. However, on the right-hand side of the boundary, the other set of lamellae impinges upon the central plane at an angle so that the repeat distance is $L/\cos(\varphi + \theta/2)$. In the T-junctions shown in Figures 1c, 3c, and 11, where $\theta \approx 90°$ and $\varphi \approx 45°$, there is no way for the lamellae to match across the boundary since the repeat spacing on one side is infinite. In Figure 11, on the right-hand side of the boundary the geometry is pure T. However, proceeding to the left both the tilt angle and asymmetry of the boundary decrease due to a slight curvature in the boundary itself and also due to the presence of the previously discussed omega tilt boundary. On the left-hand side the boundary thus becomes a chevron. In the intermediate region between the pure T-geometry on the right and the chevron on the left, some of the lamellar planes make it around in a chevron-like bend and some end in cylindrical caps as in the T-junction. In this transition region, proceeding from the chevron to the T-junction, first the chevron and T-like planes alternate, then there are two T-planes between chevron planes, and finally there are only T-planes. Notice that the chevron-like lamellae in this transition region possess some omega character. This is to be expected for chevron boundaries of approximately 90° tilt.

Finally, note that Figure 2c also shows a transition from an omega tilt boundary to the T-junction morphology. Throughout this boundary the tilt angle is the same, approximately 90°. The left-hand part of the boundary where the omega morphology is observed is approximately symmetric. However, due to the curvature of the boundary itself, proceeding to the right the boundary becomes more asymmetric. This again leads to a transition to the T-junction morphology in the right-hand portion which has the pure T geometry.

Tilt Boundary Discussion and Summary

The transition from the chevron to the omega boundary type occurs as tilt is increased at constant boundary width or as boundary width is decreased at constant tilt angle. The transition from either the chevron or the omega boundary to the T-junction occurs as the boundary becomes more asymmetric, i.e., as φ increases. The fact that these transitions occur progressively through intermediate type boundaries has been demonstrated by TEM micrographs in which the transitions are seen to occur across the boundaries as boundary width or φ changes. These transitions are driven by the need to satisfy the geometrical constraints of the boundaries. In approximately symmetric tilt boundaries, increasing θ requires an ever larger lamellar spacing at the center of the boundary, the midpoint of the bend that the lamellae make across the boundary. This eventually leads to the formation of a perturbation which grows to become the semicylindrical protrusion observed in the omega morphology. The continuous nature of the change in the geometrical

requirements of lamellar spacing with increasing tilt angle leads to the continuous morphological transition that is observed. By analogy to thermodynamic phase transitions, this type of continuous grain boundary morphology transition might be considered second order.

Acknowledgment. We wish to thank Dr. L. J. Fetters of Exxon for synthesizing the diblock copolymers and Profs. H. Karcher, D. Hoffman, R. Kusner, and P. Smith for discussions on differential geometry. We also thank a referee for useful comments. Funding was provided by NSF DMR 8907433, AFOSR 910078, and NSF CMSE 9022933.

References and Notes

(1) Gido, S. P.; Gunther, J.; Thomas, E. L.; Hoffman, D. *Macromolecules* **1993**, *26*, 4506.
(2) Gido, S. P.; Thomas, E. L. *Macromolecules* **1994**, *27*, 849.
(3) Alward, D. B.; Kinning, D. J.; Thomas, E. L.; Fetters, L. J. *Macromolecules* **1986**, *19*, 215.
(4) Kinning, D. J.; Thomas, E. L.; Ottino, J. M. *Macromolecules* **1987**, *20*, 1129.
(5) Gido, S. P.; Thomas, E. L. In Preparation.
(6) Kléman, M. *Points, Lines, and Walls*; John Wiley and Sons: New York, 1983.
(7) Williams, C. E.; Kleman, M. *J. Phys. Colloq.* **1975**, *36*, 315.
(8) Wang, Z. G.; Safran, S. A. *J. Chem. Phys.* **1991**, *94*, 679.
(9) Wang, Z.-G.; Safran, S. A. *J. Phys. (Paris)* **1990**, *51*, 185.
(10) Semenov, A. N. *Sov. Phys.—JETP (Engl. Transl.)* **1985**, *61*, 733.